

Water Resources Research®

RESEARCH ARTICLE

10.1029/2022WR033142

Special Section:

Modeling, simulation, and big data techniques in subsurface fluid flow and transport

Key Points:

- A pore-throat segmentation method is proposed based on local hydraulic resistance equivalence
- The reliability and accuracy are validated via various benchmark cases
- The proposed method accurately predicts single/two-phase transport properties

Supporting Information:

Supporting Information may be found in the online version of this article.

Correspondence to:

X. Jin and M. Wang,
jinxu@petrochina.com.cn;
mrwang@tsinghua.edu.cn

Citation:

Liu, Y., Gong, W., Zhao, Y., Jin, X., & Wang, M. (2022). A pore-throat segmentation method based on local hydraulic resistance equivalence for pore-network modeling. *Water Resources Research*, 58, e2022WR033142. <https://doi.org/10.1029/2022WR033142>

Received 29 JUN 2022

Accepted 25 NOV 2022

Author Contributions:

Conceptualization: Moran Wang
Formal analysis: Xu Jin
Investigation: Yang Liu
Methodology: Moran Wang
Project Administration: Moran Wang
Resources: Yu Zhao, Xu Jin
Supervision: Moran Wang
Validation: Yang Liu, Yu Zhao
Writing – original draft: Yang Liu
Writing – review & editing: Moran Wang

A Pore-Throat Segmentation Method Based on Local Hydraulic Resistance Equivalence for Pore-Network Modeling

Yang Liu¹, Wenbo Gong¹ , Yu Zhao², Xu Jin³, and Moran Wang¹ 

¹Department of Engineering Mechanics, Tsinghua University, Beijing, China, ²Exploration & Development Research Institute, Daqing Oilfield Company, Daqing, China, ³Research Institute of Petroleum Exploration & Development of PetroChina, Beijing, China

Abstract The pore network is an approximate representation of the void space of porous materials, such as rocks and soil, via pores (corresponding to large cavities) and throats (narrow constrictions). During extraction of networks from real void space, ambiguous definitions or determinations of pores and throats may cause significant errors in the prediction of single/multi-phase transport properties. Meanwhile, the pore-throat segmentation needs to exclude non-physical parameters as much as possible. In this work, we propose a pore-throat segmentation method based on local hydraulic resistance equivalence between the real void space and the simplified pore-throat geometry. Each pore-throat interface is carefully determined at the position where the simplified tubes preserve the local hydraulic resistance of the real space best. This local segmentation method ensures equivalency between extracted pore network and real pore space without any empirical or non-physical parameters. After validations of accuracy and reliability by benchmarks, this method is applied to real porous materials including spherical pack, sand pack, sandstone, limestone, and carbonate. The single/two-phase transport properties predicted by the new method agree well with the experimental data and the direct simulation results. The proposed method improves the accuracy of pore network model (PNM) predictions significantly with a slight increase in computational cost. This local pore-throat segmentation method may enhance the capability of PNM for more complicated applications.

1. Introduction

Multiphase flow in porous media is ubiquitous in nature and industrial processes, such as hydrocarbon recovery (Blunt, 2017; Chen et al., 2021; Huppert & Neufeld, 2014; Liu & Wang, 2020; Singh et al., 2019), aquifer management (Gerke et al., 2015; Godinho et al., 2016; Rubol et al., 2016; Yang et al., 2022), reactive transport (Chiogna & Rolle, 2017; Mehmani & Xu, 2022; Wang & Battiato, 2020; Xiong et al., 2016), and engineering designs of fuel cells (Gholipour et al., 2021; Tranter et al., 2018). To understand these processes, pore-scale modeling is widely used to connect microscale mechanisms to macroscopic properties. Pore-scale modeling methods for multiphase flow in porous media can be divided into two categories (Blunt et al., 2013; Meakin & Tartakovsky, 2009): direct numerical simulations (DNS) and network simulations. DNS solve the governing equations of flow and other transports directly on the porous structures, using such as finite volume methods (FVM) (Ferrari & Lunati, 2014), lattice Boltzmann methods (LBM) (Alizadeh et al., 2019; Chen & Doolen, 1998; Chen et al., 2019; Ramstad et al., 2010; Xie et al., 2021; Zheng et al., 2018), smoothed particle hydrodynamics (SPH) methods (Tartakovsky et al., 2007), dissipative particle dynamics (DPD) methods (Dzwinel & Yuen, 2000) and so on. DNS require details of complex microstructures of permeable media to account for the effect of viscous forces so they are generally computationally expensive. It has been recently reported that DNS limits to a domain size up to 700^3 to the best of personal computational resources (Gerke et al., 2020). An alternative solution to pore-scale modeling is the pore network model (PNM), which simulates the fluid flow and transport on a representative network with simplified elements derived from the void space. Since the complex pore structures of real materials are simplified as network elements, the transport properties of a pore or throat can be calculated analytically or semi-analytically. Consequently, the PNM is computationally efficient and can deal with a much larger computation domain than any DNS method with a given computational resource.

The pore network modeling contains two core processes, network construction and transport modeling. The network can be either extracted from pore space for real applications or generated artificially for mechanism study. In recent years, exciting developments have been made in algorithms for PNMs (Chen et al., 2021; Mehmani & Xu, 2022; Qin et al., 2022; Xie et al., 2017), yet, the efforts paid to network extraction from real pore space, which

is the basis of pore network modeling for real applications, are still not enough. In the early studies of PNMs, regular networks (Chatzis & Dullien, 1977; Jerauld & Salter, 1990) were mostly adopted. Nevertheless, it was generally believed that regular networks fail to reflect the real topology and geometry of rock pore space (Blunt et al., 2013) and a pore network representative of porous structures is the prerequisite for reliable simulation results (Wang et al., 2020). Therefore, researchers came up with a way to extract networks directly from the pore space, typically from scanned images. Extracting a network from an image generally may involve three steps. The first step is to locate the centers of pores and throats using an effective algorithm, such as medial axis algorithms (Lindquist et al., 1996), maximal ball algorithms (Dong & Blunt, 2009), or watershed algorithms (Gostick, 2017). The void space is then divided into pore regions separated by interfaces located at the throat centers. In the second step, the pore-throat segmentation is performed for each “pore₁-throat-pore₂” link. Consequently, each voxel in the image is assigned to a unique pore or throat. The final step is to calculate network attributes such as volume, conduit length, and shape factor.

As for the determination of pore and throat centers, numerous algorithms have been proposed over the past three decades. Zhao et al. (1994) developed the multi-orientation scanning approach to locate pore necks (throats) by slices of a 3D volume in multi orientations. Lindquist et al. (1996) put forward the medial axis algorithm that transformed the pore space into a medial axis by a burning algorithm. The medial axis represents the topological skeleton of the pore space, along which pores and throats are located at conjunction nodes and local minima, respectively. The medial axis-based method mathematically preserved the topology of pore space, however, it defined the centers of pores and throats a little bit ambiguously, especially for images with high noise or complicated geometries. The maximal ball method was originally proposed by Silin et al. (2003), and then improved by several contributors (Al-Kharusi & Blunt, 2007; Arand & Hesser, 2017; Dong & Blunt, 2009). In the maximal ball method (Dong & Blunt, 2009), the first step is to build the maximal inscribed sphere at each voxel; those spheres included in others are removed; then, through a clustering procedure, centers of masters and common child define the centers of pores and throats, respectively. Another method is the watershed segmentation of the pore space. The watershed method was first investigated by Sheppard et al. (2006) and Thompson et al. (2008) and was substantially improved later (Gostick, 2017; Rabbani et al., 2014). The first step of the watershed method (Gostick, 2017) is to calculate the distance map of the pore space; next, identify peaks in the distance map. The void space is then divided into different pore regions by the watershed algorithm. Each pore region corresponds to a single pore, and the interface where pore regions come into contact defines a throat center.

After pore regions and throat centers are recognized from the real pore space, we need to specify what constitutes pores and throats, that is, the pore-throat segmentation which is the crucial part of pore network construction. Several methods have been developed for pore-throat segmentation, which appear empirical because the exact physical definitions of pore and throat are still lacking (Bhattad et al., 2011; Xiong et al., 2016). Øren and Bakke (2003) proposed a method to calculate the conduit lengths of pores and throats with a segmentation coefficient α . The pore lengths, l_i and l_j , are given by

$$l_i = l'_i \left(1 - \alpha \frac{r_i}{r_t} \right), \quad (1)$$

$$l_j = l'_j \left(1 - \alpha \frac{r_j}{r_t} \right), \quad (2)$$

where l'_i and l'_j are the Euclidean distances from the centers of pore i and pore j to the throat center; r_i , r_j , and r_t are the radii of pore i , pore j , and throat, respectively. The throat length is defined as

$$l_t = l_{ij} - l_i - l_j, \quad (3)$$

where l_{ij} is the Euclidean distance between two adjacent pores. The method was subsequently followed by Dong and Blunt (2009). In the original work of Øren and Bakke (2003), α was taken as 0.5, whereas 0.6 was used by Dong and Blunt (2009). For convenience, this method is abbreviated as “ α method” in the following text. Later, Sholokhova et al. (2009) proposed a similar method to calculate conduit lengths,

$$l_i = l'_i(1 - w), \quad (4)$$

$$l_j = l'_j(1 - w), \quad (5)$$

$$l_i = w \cdot l_{ij}, \quad (6)$$

where w is the segmentation coefficient. Unlike the α method, there is no recommended value for w . This method is abbreviated as “ w method” in the following parts of this paper. The coefficient, either α or w , exhibits non-physical, empirical, and sometimes arbitrary, which may result in uncertain or even counterintuitive simulation results (Bondino et al., 2013; Gerke et al., 2020; Idowu et al., 2013). Youssef et al. (2007) proposed a method to calculate the effective throat length combined with the medial axis method. Pores had zero lengths while the effective throat length was defined as

$$l_{\text{eff},t} = \sum_{i=1}^{n_{\text{max}}} l_i \left(\frac{r_t}{r_i} \right)^4, \quad (7)$$

where n_{max} was the number of elements along the medial axis between pores, and r_t was the throat radius. r_i and l_i were the radius and length of the i^{th} element. This method pioneered the estimation of effective throat length based on flow resistance, however, a relative error of 38.4% in absolute permeability prediction was reported (Youssef et al., 2007). This method is abbreviated as “Youssef method” in the following parts of this work. Yi et al. (2017) calculated the effective throat length by simplifying the complex pore structures as capillary tubes whose radii vary linearly along the axes. Zheng et al. (2019) calculated the conduit length by subtracting the radius from the Euclidean distance between two pores. The conduit length was then combined with an effective throat radius to obtain hydraulic conductance. All the methods mentioned above, whether containing non-physical parameters or not, do not specify how the pores and throats constitute the void space. Consequently, the volume determinations of pores and throats still exhibit non-physical or arbitrary, which may result in large errors, especially in multi-phase flow simulations. Hence, a physics-based algorithm for pore-throat segmentation is urgently needed.

To overcome the empirical and non-physical effects of the previous methods, a few attempts have been made to combine the traditional pore-throat segmentation methods with DNS. It may be natural to determine the boundary position between a pore and a throat rather than to calculate the effective conduit length. Sheppard et al. (2005) tried to determine the pore-throat boundaries using DNS for two-phase flow in the pore space. The interface between the wetting phase and the non-wetting phase was used to define the boundary between pore and throat under a certain condition. Raeini et al. (2017) developed another segmentation method where a “half throat” concept was proposed and the conductance of each “half throat” was calculated by single-phase DNS. Nevertheless, DNS is too computationally expensive and increases extremely the costs of PNM. Thus, an efficient method for pore-throat segmentation is another crucial demand to obtain a representative network for PNM.

In this work, we are to propose a new pore-throat segmentation method based on local hydraulic resistance equivalence between the simplified pore-throat geometry and real pore space to exclude any non-physical parameters in pore network modeling. This method segments the void space and specifies the voxels exactly belonging to a pore or a throat, and hence the conduit lengths and volumes of pores and throats are physically determined simultaneously. The accuracy and reliability of this method will be validated by standard or real cases. The single-phase transport properties, like absolute permeability, and two-phase transport properties, such as the capillary pressure curve and the relative permeability curves, will be predicted by the new framework of PNM and the results will be compared with the experimental data or DNS results. The performance of the proposed method will be analyzed and discussed in the following sections.

2. Methods and Validations

There are four steps in the proposed pore-throat segmentation algorithm: (a) to identify each pore region and interface in the void space; (b) to partition pore regions into pore and throat and calculate the size of pore and throat based on local hydraulic resistance equivalence; (c) to correct the conduit length based on local resistance if the flow pathway is tortuous; (d) to calculate the other network properties for a complete pore-network modeling. The details of the algorithm are introduced as follows.

2.1. Identification of Pore Regions and Throat Centers

The subnetwork of the over-segmented watershed algorithm proposed by Gostick (2017), abbreviated as SNOW, is adopted in this work for identifying pore regions and throat centers due to its advantages of robust cross-section detection, ease of secondary developments, and wide applicability to porous media with various porosity. The network extraction is initiated by loading the binary image into memory, where “1” represents void and “0” represents solid, respectively, so that a distance map of the pore space is obtained. The discretized nature of binary images will result in plateaus in the distance map, which may be wrongly recognized as peaks in the subsequent step. Thus, a Gaussian blur filter is used to remove these problematic plateaus. The value of sigma in the Gaussian blur filter will make difference to the number of local maxima. In this work, the value is 0.35, which follows the practice of Gostick (2017).

Next, peaks, namely the local maxima, are identified by applying a maximum filter with a spherical structuring element to the smoothed distance map. Peaks are marked as “True” values in a Boolean mask. However, the size of the structuring element R_s affects the number of peaks. Many spurious peaks may be generated if R_s is too small. Following the previous setting parameters of Gostick (2017), R_s is taken as 5. Despite of careful parameter selection, there are inevitably large quantities of spurious peaks. Then, a special step is performed to remove peaks on the saddles or to merge peaks that are too close together.

The above steps create a set of markers, which is passed to a marker-based watershed algorithm to obtain pore regions. Each pore region corresponds to a single pore, and the interface with the minimal distance separating pore regions corresponds to a throat center. The voxels in a pore region are labeled with the same number, representing the pore index. The connectivity is determined by scanning pore indexes in the shell of adjacent voxels.

2.2. Pore-Throat Segmentation

In the previous stage, the sizes of pores and centers of throats, and their connectivity have been identified, which characterize the topological and geometric features of the void space. The next step is to locate boundaries between pores and throats through physics-based pore-throat segmentation. Specifically, the hydraulic conductance, in other words, the flow resistance, of simplified geometries in the PNM should be as close as possible to that of real structures of the void space. The question is how to calculate the local flow resistance between two adjacent pores in the void space. The first solution lies in the various DNS methods, such as FVM, LBM, etc. Yet, DNS is computationally expensive and runs counter to the intention of PNM for high computational efficiency. To trade off the accuracy and efficiency of calculating the flow resistance between pores, the following assumptions are made.

1. The cross-sectional shape remains constant along the path from the throat center to the pore center.
2. The hydraulic conductivity of each cross-section along the path is proportional to the fourth power of the hydraulic radius.
3. The total flow resistance from one throat center to its adjacent pore center can be obtained by integrating the flow resistance of each cross-section with an infinitesimal length (Sochi, 2013).

To be noted, the contribution of cross-sectional variation on the total flow resistance is not considered here, which may under- or over-estimate slightly the resistance and will be discussed in Text S1 in Supporting Information S1. These assumptions are acceptable for flows under a low Reynolds number. Based on assumption 3, each “pore₁-throat-pore₂” link can be split into two parts of “throat-pore₁” and “throat-pore₂,” as Figure 1 shows. The “throat-pore₁” part is taken as an example to illustrate the hydraulic resistance-based segmentation.

The total hydraulic resistance based on assumption 3 at a low Reynolds number is given by

$$W_{\text{tot}} = C \cdot \mu \cdot \int \frac{1}{r_{(x)}^4} dx, \quad (8)$$

where $r_{(x)}$ is the radius of the maximal inscribed ball at location x , μ is the viscosity, and C is a constant related to the cross-sectional shape.

In the voxel-based image, the flow path is composed of several longitudinal sections. Equation 8 can be approximated by

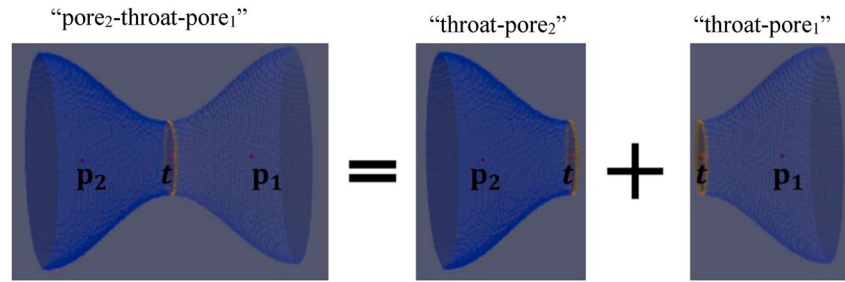


Figure 1. A schematic of a “pore₂-throat-pore₁” link, where p_1 , p_2 , and t stand for the centers of pore₁, pore₂, and throat, respectively.

$$W_{\text{tot}} = C \cdot \mu \cdot \sum_s \frac{\Delta l_s}{r_{(s)}^4}, \quad (9)$$

where $r_{(s)}$ and Δl_s represent the hydraulic radius and the length of the section s , respectively. The $r_{(s)}$ is determined as the maximal distance value corresponding to voxels in section s .

When the length of every section Δl_s takes one voxel size, the minimal size in a binary image, Equation 9 gives the best approximation to the total flow resistance. Therefore, a layer-by-layer dilation algorithm is adopted to obtain the hydraulic radius of each section. The dilation process is detailed as follows.

First, the hydraulic radius of the first section is found as the maximal distance value corresponding to voxels at the throat center. These voxels become the initial seeds for dilation and then expand a layer of one voxel toward the pore₁.

Next, the newly involved voxels form a new section and the hydraulic radius is analogously determined by the distance value. The new section continues to expand a layer of one voxel toward the pore₁.

The dilation process continues until the center of pore₁ is involved, as shown in Figure 2c. The dilation index is used to label the voxels in each section. For example, the voxels in the first section are labeled as 0, and those in the second section are labeled as 1, etc. The dilation index and hydraulic radius of each section are recorded. Based on the hydraulic radii of different sections, the total flow resistance is calculated by Equation 9.

During the dilation process, each section is a potential choice for the boundary between the throat and the pore₁. Each potential boundary results in one conduit length of the simplified geometry in the PNM. The simplified geometry consists of two cylindrical tubes with the same radii as the throat and the pore₁, respectively. For each potential segmentation, the hydraulic resistance of the simplified geometry in the PNM is calculated by

$$W_{\text{PNM}} = C \cdot \mu \cdot \Delta l_s \cdot \left(\frac{N_{s_b}}{R_t^4} + \frac{N_{\text{max}} - N_{s_b}}{R_p^4} \right), \quad (10)$$

where R_p and R_t are the radii of pore₁ and throat, respectively. N_{max} and N_{s_b} are the dilation indexes of the last section and the chosen boundary section, respectively. The relative error between the flow resistance of the simplified geometry in PNM and the total flow resistance of “throat-pore₁” is

$$\Delta E = \frac{|W_{\text{PNM}} - W_{\text{total}}|}{W_{\text{total}}} = \frac{\left| \sum_s \frac{1}{r_{(s)}^4} - \left(\frac{N_{s_b}}{R_t^4} + \frac{N_{\text{max}} - N_{s_b}}{R_p^4} \right) \right|}{\sum_s \frac{1}{r_{(s)}^4}}. \quad (11)$$

The boundary s_{b1} between the throat and the pore₁ in “throat-pore₁” is defined as the section that minimizes the relative error ΔE among all sections. The voxels whose dilation index smaller than that of the boundary belong to the throat, and the rest belong to the pore₁. The boundary s_{b2} between the throat and the pore₂ in “throat-pore₂” can be similarly determined. The voxels belonging to the throat in both “throat-pore₁” and “throat-pore₂” constitute the whole throat, as shown in Figure 2e. The above operations are performed for the whole void space.

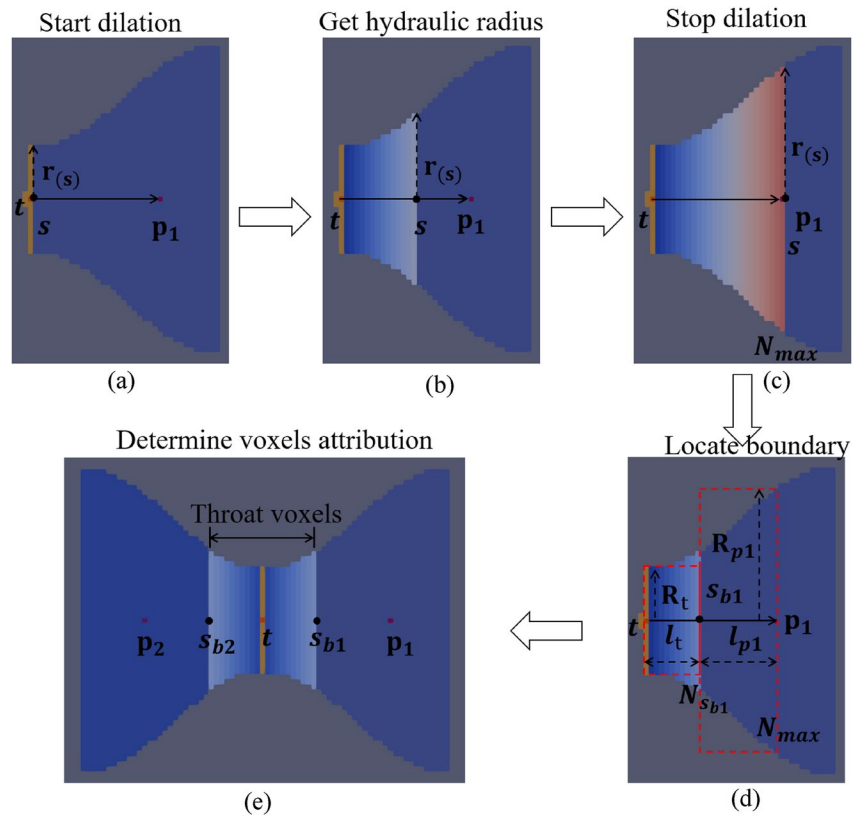


Figure 2. Illustration for local hydraulic resistance equivalence-based pore-throat segmentation. The simplified geometry in pore network model is represented with the red dashed line. The voxels are rendered by their dilation indexes, where the larger number corresponds to the redder color. For easy understanding, the $r(s)$ is the geometric radius in the intuitive sense instead of the closest distance to the wall.

2.3. Tortuous Corrections of Conduit Lengths

Due to the tortuous nature of pore structures, the dilation direction may deviate from the medial axis. To reduce the impact of this factor on conduit lengths, the pore₁ length l_{p1} and the throat partial length l_{t1} in “throat-pore₁” are calculated by

$$l_{t1} = \frac{N_{s_{b1}}}{N_{\max}} l_{p1,t}, \quad (12)$$

$$l_{p1} = \frac{N_{\max} - N_{s_{b1}}}{N_{\max}} l_{p1,t}, \quad (13)$$

where $l_{p1,t}$ is the Euclidean distance between the pore₁ center and the throat center. $N_{s_{b1}}$ and N_{\max} are dilation indexes of the boundary section s_{b1} and the last section in “throat-pore₁,” respectively. The pore₂ length l_{p2} and the throat partial length l_{t2} in “throat-pore₂” can be similarly determined.

2.4. Other Network Attributes Calculations

The radius is determined by the distance value at the center of a pore or a throat. The throat shape factor is calculated by Bultreys et al. (2018), Mason and Morrow (1991)

$$G = \frac{R^2}{4A}, \quad (14)$$

where R represents the throat radius and A is the cross-sectional area at the throat center. For pores, the shape factor is calculated by the definition of Dong and Blunt (2009).

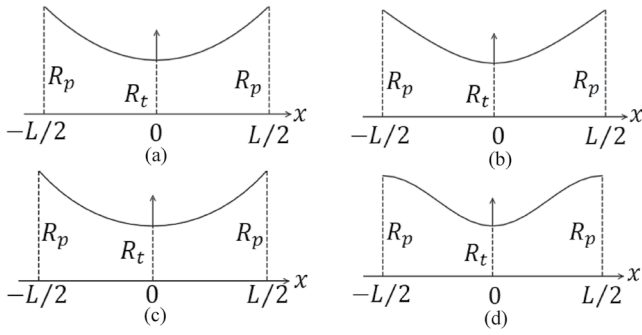


Figure 3. Schematic diagrams of longitudinal profiles of simplified capillary tubes: (a) a parabolic tube, (b) a hyperbolic tube, (c) a hyperbolic cosine tube, and (d) a sinuous tube. R_p is the pore radius, R_t is the throat radius, and L is the length of the tube.

The whole throat length l_t is the sum of the throat partial lengths, namely, l_{t1} in “throat-pore₁” and l_{t2} in “throat-pore₂.”

$$l_t = l_{t1} + l_{t2}. \quad (15)$$

The volume of a pore/throat is determined by counting the number of voxels within it.

2.5. Benchmarks

Simple structures are used to validate the proposed method for pore-throat segmentation. To mimic the pore structures in granular porous media, tubes with a parabolic profile, hyperbolic profile, hyperbolic cosine profile, and sinusoidal profile are adopted as shown in Figure 3. Schematic representations of the geometries and the corresponding pressure drops are presented as follows.

The analytical flow resistance W_{ana} of a parabolic tube is expressed as (Sochi, 2013):

$$W_{ana} = \frac{4\mu L}{\pi(R_p - R_t)} \left[\frac{1}{3R_t R_p^3} + \frac{5}{12R_t^2 R_p^2} + \frac{5}{8R_t^3 R_p} + \frac{5 \operatorname{atan}\left(\sqrt{\frac{R_p - R_t}{R_t}}\right)}{8R_t^{3.5} \sqrt{R_p - R_t}} \right]. \quad (16)$$

The analytical flow resistance W_{ana} of a hyperbolic tube is expressed as (Sochi, 2013)

$$W_{ana} = \frac{4\mu L}{\pi} \left[\frac{1}{R_t^2 R_p^2} + \frac{\operatorname{atan}\left(\sqrt{\frac{R_p^2 - R_t^2}{R_t^2}}\right)}{R_t^3 \sqrt{R_p^2 - R_t^2}} \right]. \quad (17)$$

The analytical flow resistance W_{ana} of a hyperbolic cosine tube is calculated by Sochi (2013)

$$W_{ana} = \frac{8\mu L}{3\pi R_t^4} \left[\frac{\tanh\left(\operatorname{acosh}\left(\frac{R_p}{R_t}\right)\right) \left[\operatorname{sech}^2\left(\operatorname{acosh}\left(\frac{R_p}{R_t}\right)\right) + 2 \right]}{\operatorname{acosh}\left(\frac{R_p}{R_t}\right)} \right]. \quad (18)$$

The analytical flow resistance W_{ana} of a sinuous tube is given by Sochi (2013)

$$W_{ana} = \frac{\mu L}{2\pi(R_p R_t)^{3.5}} \cdot \left[2(R_p + R_t)^3 + 3(R_p + R_t)(R_p - R_t)^2 \right]. \quad (19)$$

The aspect ratio γ and pore-throat size ratio β are defined as

$$\gamma = \frac{L}{R_t}, \quad (20)$$

$$\beta = \frac{R_p}{R_t}. \quad (21)$$

The structures above are completely controlled by the throat radius R_t , the aspect ratio γ , and the pore-throat size ratio β . That is to say, a combination of (R_t, γ, β) determines a unique structure. Structures with a wide range of variation, with R_t from 10 to 20, γ from 5 to 30, and β from 2 to 10, are used for benchmarks. The proposed

Table 1
Properties of the Studied Samples

Samples	Types	Resolution (μm)	Size (voxels)	Porosity (%)
Berea ^a	Sandstone	5.345	400 ³	19.6
S1 ^a		8.683	300 ³	14.1
S2 ^a		4.956	300 ³	24.6
S3 ^a		9.10	300 ³	16.9
S4 ^a		8.96	300 ³	17.1
S5 ^a		3.997	300 ³	21.1
S6 ^a		5.1	300 ³	24.0
S7 ^a		4.803	300 ³	25.0
S8 ^a		4.892	300 ³	34.0
S9 ^a		3.398	300 ³	22.2
C1 ^a	Carbonate	2.85	400 ³	23.3
C2 ^a		5.345	400 ³	16.8
A1 ^a	Sand pack	3.85	300 ³	42.9
SP1 ^b	Spherical pack	5.0	290 × 300 × 310	15.7
SP2 ^b		5.0	290 × 300 × 310	27.4
SP3 ^b		5.0	290 × 300 × 310	41.4
SP4 ^c		5.0	297 × 287 × 256	29.2
SP5 ^c		5.0	289 × 281 × 977	34.0
SP6 ^c		5.0	289 × 279 × 988	34.7

^aThe core samples are cited from Dong and Blunt (2009). ^bThe samples are generated by the polydisperse_spheres module in the open-source package Porespy (Gostick et al., 2019). ^cThe samples are generated using the open-source discrete element software Yade (Šmilauer et al., 2015).

calculation of effective throat lengths in the Youssef method is described in Text S3 in Supporting Information S1. In addition, the networks extracted by the maximal ball algorithm with $\alpha = 0.6$ (Dong & Blunt, 2009) are also considered here. In total, five types of networks are included, they are WS – HC, WS – Youssef, WS – w , WS – α , and MB – α , and the corresponding methods are shown in Table 2. In all of WS – Youssef networks, WS – w networks, and WS – α networks, volumes are only assigned to pores, that is, volume of throats is zero. Conduit lengths and volumes of network elements are compared among different types of networks. Furthermore, the single-phase and two-phase flow are simulated based on the networks. The predicted transport properties are verified against the numerical solutions or the experimental data.

Table 2
Different Types of Networks and Corresponding Methods

Network types	Description
WS – HC (present)	Watershed algorithm ^a + the present method
WS – Youssef	Watershed algorithm ^a + the Youssef method
WS – w	Watershed algorithm ^a + w method ($w = 0.3$)
WS – α	Watershed algorithm ^a + α method ($\alpha = 0.6$) ^b
MB – α	Maximal ball algorithm ^c + α method ($\alpha = 0.6$) ^b

^aThe SNOW proposed by Gostick (2017). ^b $\alpha = 0.6$ is cited from Dong and Blunt (2009). ^cThe Maximal ball algorithm proposed by Dong and Blunt (2009).

method is applied to the structures for pore-throat segmentation. The flow resistance in the PNM W_{PNM} can be obtained by Equation 9 with $C = \frac{8}{\pi}$.

Hydraulic conductance in the PNM, the inverse of flow resistance, is compared with the analytical solution in dimensionless form,

$$K'_{\text{ana}} = \frac{1/W_{\text{ana}}}{K_0}, \quad (22)$$

$$K'_{\text{PNM}} = \frac{1/W_{\text{PNM}}}{K_0}, \quad (23)$$

where

$$K_0 = \frac{\pi R_p^4}{8\mu L}. \quad (24)$$

The results prove the reliability of our method for pore-throat segmentation (also see Figure S7 in Supporting Information S1).

3. Results and Discussion

The presented segmentation method is applied to a variety of permeable materials, including 6 spherical packs, 1 sand pack, 15 sandstones, 1 limestone, and 2 carbonates. To ensure universality, two distinct programs (Gostick et al., 2019; Šmilauer et al., 2015) are used to generate the spherical packs. The properties of the studied samples are summarized in Tables 1 and 4. For comparison, the α method and the w method coupled with the SNOW algorithm (Gostick, 2017) are applied to extract pore networks, with segmentation coefficient $\alpha = 0.6$ (Dong & Blunt, 2009) and $w = 0.3$, respectively. The value of 0.3 is selected for w due to the smallest average error in the predicted absolute permeability, which is detailed in Text S2 in Supporting Information S1. As a representative method for the estimation of effective throat lengths, the Youssef method is also involved in the comparison. The

calculation of effective throat lengths in the Youssef method is described in Text S3 in Supporting Information S1. In addition, the networks extracted by the maximal ball algorithm with $\alpha = 0.6$ (Dong & Blunt, 2009) are also considered here. In total, five types of networks are included, they are WS – HC, WS – Youssef, WS – w , WS – α , and MB – α , and the corresponding methods are shown in Table 2. In all of WS – Youssef networks, WS – w networks, and WS – α networks, volumes are only assigned to pores, that is, volume of throats is zero. Conduit lengths and volumes of network elements are compared among different types of networks. Furthermore, the single-phase and two-phase flow are simulated based on the networks. The predicted transport properties are verified against the numerical solutions or the experimental data.

3.1. Comparison of Throat Lengths and Volumes

Conduit lengths and volumes of network elements have significant impacts on predicted single-phase and multiphase transport properties (Bhattad et al., 2011; Bondino et al., 2013; Gostick, 2017; Idowu et al., 2013; Raeini et al., 2017; Xiong et al., 2016). As a direct result of pore-throat segmentation, the throat lengths of networks with different segmentation methods are quantitatively compared. The dimensionless throat length (L'_i) is used

$$L'_i = \frac{L_i}{\Delta L}, \quad (25)$$

where L_i is the real throat length and ΔL is the size of one voxel.

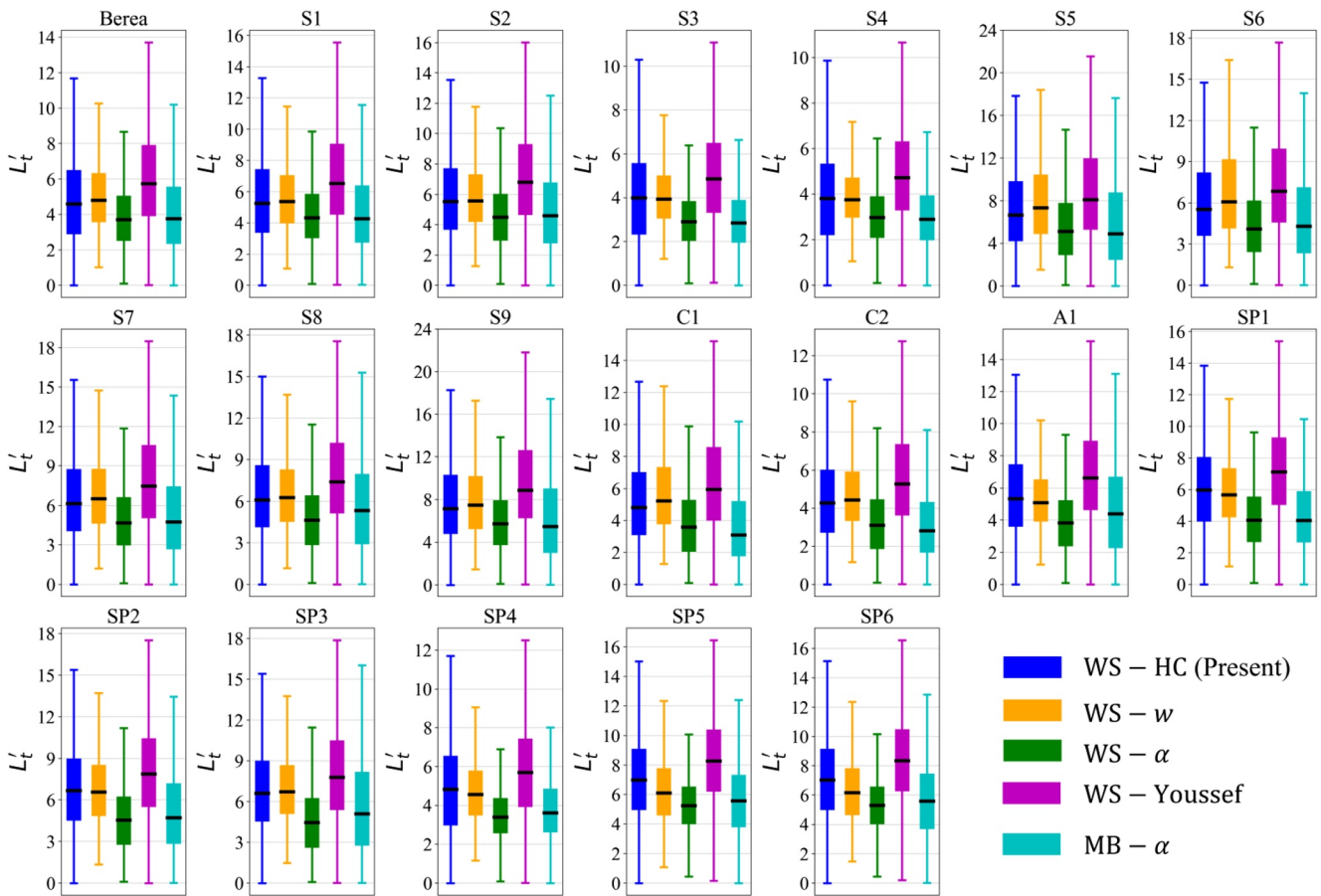


Figure 4. Box plots of dimensionless throat length L'_t , samples including sandstone (Berea and S1–S9), carbonate (C1–C2), sand pack (A1), and spherical pack (SP1–SP6). The bold black line in the colored box indicates the median value, and the lower and upper boundaries of the colored box indicate the first quartile and the third quartile. The bottom and top whiskers represent the minimum and maximum values in the data set excluding any outliers, respectively. Outliers are not shown in the figures. The WS – Youssef networks, WS – w networks, and WS – α networks are extracted by the Youssef method, the w method, and the α method coupled with the SNOW algorithm (Gostick, 2017), respectively. The MB – α networks are extracted by the α method coupled with the maximal ball algorithm (Dong & Blunt, 2009).

As shown in Figures 4 and 5, different types of networks vary greatly in terms of throat length. WS – α networks have the most concentrated distributions and smallest median values of throat lengths, while the other three networks have very scattered throat length distributions.

Volumes of network elements are compared in Figure 5b. In the present method, the volume of a pore or throat is calculated by counting the number of voxels within it, whereas in other methods, volumes are only assigned to pores, that is, throat volumes are zero. Volumes of elements in different types of networks are compared in dimensionless form as

$$V'_e = \frac{V_e}{\Delta L^3}, \quad (26)$$

where V_e is the volume of an element and ΔL is the size of one voxel.

As shown in Figure 5b, WS – HC networks have a more uniform distribution and smaller median values of volumes of network elements, compared to the other types of networks.

3.2. Single-Phase Flow

Absolute permeability, as the most important property of porous media, is used to verify the accuracy of the proposed method. For different types of networks, the absolute permeability is calculated and verified against

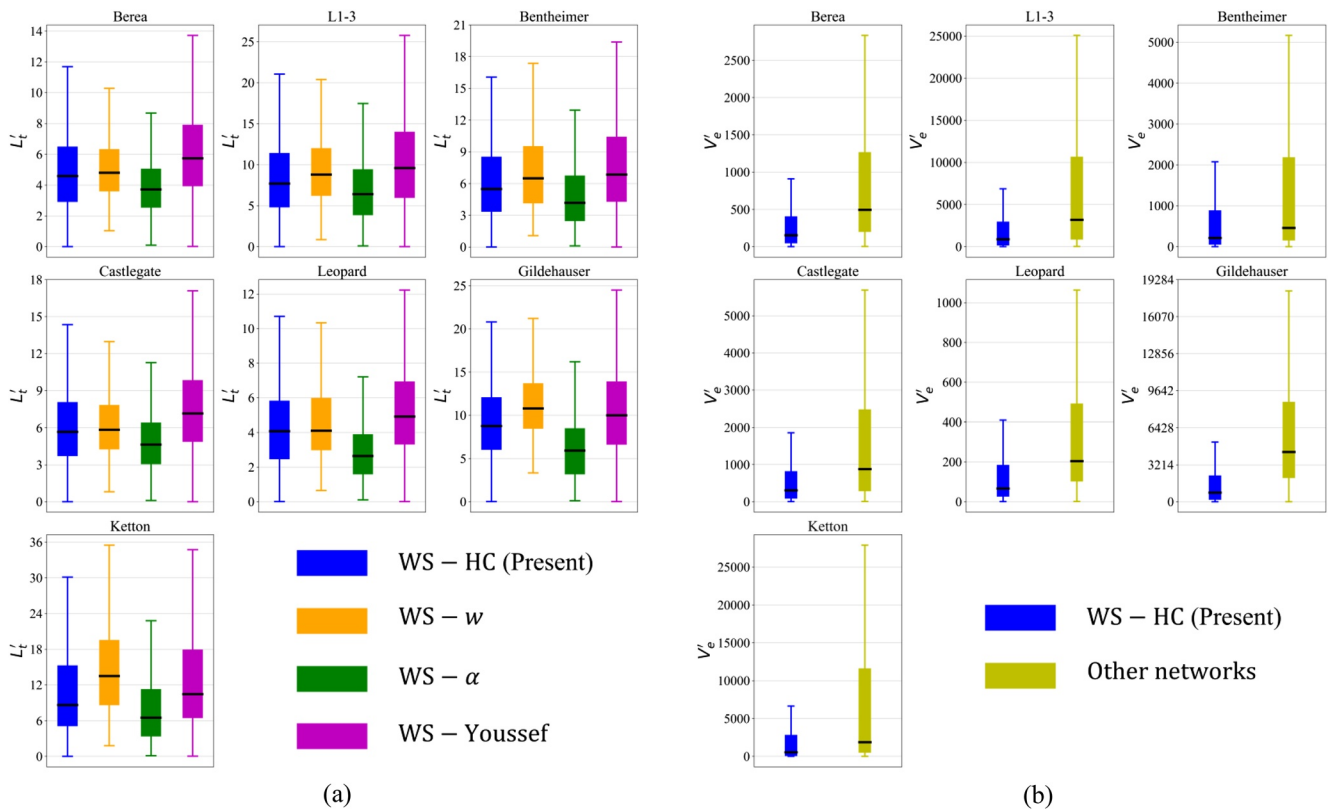


Figure 5. Box plots of (a) dimensionless conduit lengths L_e^* , and (b) dimensionless volumes V_e^* of network elements for the samples involved in two-phase simulation. The bold black line in the box indicates the median value, and the lower and upper boundaries of the box indicate the first quartile and the third quartile. The bottom and top whiskers represent the minimum and maximum values in the data set excluding any outliers, respectively. Outliers are not shown in the figures. The WS – Youssef networks, WS – w networks, and WS – α networks are extracted by the Youssef method, the w method, and the α method coupled with the SNOW algorithm (Gostick, 2017), respectively. The “other networks” in the right figure include the WS – Youssef networks, the WS – w networks, and the WS – α networks.

the numerical solutions by LBM simulations in this work, which are based on an open-source program MF-LBM (Chen et al., 2019).

In the PNM, the hydraulic conductance of an individual element is (Øren et al., 1998; Patzek & Silin, 2001)

$$g = \frac{kGA^2}{\mu l}, \quad (27)$$

where A is the cross-sectional area, l is the conduit length, and k is a coefficient dependent on cross-sectional shape. For ducts with triangle, square, and circle shapes, k is 0.6, 0.5623, and 0.5, respectively. The conductance between two adjacent pores is given by the harmonic mean of conductance in each element,

$$g_{ij} = \frac{1}{\frac{1}{g_i} + \frac{1}{g_t} + \frac{1}{g_j}}, \quad (28)$$

where t indicates the throat, and i and j represent pores. With a pressure difference of $(P_i - P_j)$, the flow rate between i and j is given by

$$q_{ij} = g_{ij}(P_i - P_j). \quad (29)$$

With a pressure drop ΔP between the inlet and outlet, the pressure field and then the total flow rate q_{ts} can be obtained by imposing mass conservation at every pore. The absolute permeability is calculated using Darcy's law,

$$K = \frac{q_{ts}\mu L}{A_0\Delta P}, \quad (30)$$

Table 3
The Predicted Absolute Permeability of the Studied Samples

Samples	K_x (mD)		K_y (mD)		K_z (mD)		K_{ave} (mD)					
	LBM	WS-HC	LBM	WS-HC	LBM	WS-HC	LBM	WS-HC	WS-Youssef	WS- w	WS- α	MB- α
Berea	1,876	1,860	1,805	1,729	1,658	1,719	1,780	1,769	1,727	1,632	2,406	1,111 ^a
S1	2,753	2,898	2,535	2,734	1,984	1,967	2,424	2,533	2,461	2,292	3,324	1,486 ^a
S2	5,236	5,405	4,799	4,947	4,260	4,967	4,765	5,106	4,906	5,277	6,740	3,950 ^a
S3	798	663	1,204	1,080	730	673	911	805	775	687	1,256	281 ^a
S4	581	503	610	537	415	336	535	459	445	385	705	169 ^a
S5	6,093	6,572	6,383	6,003	6,347	6,663	6,274	6,413	6,117	6,845	8,893	5,369 ^a
S6	17,134	19,617	14,222	13,536	13,417	12,225	14,924	15,126	14,407	14,969	21,543	11,282 ^a
S7	9,280	10,490	10,184	10,391	7,559	8,344	9,008	9,742	9,180	10,070	13,588	7,926 ^a
S8	15,433	15,753	16,081	16,285	15,178	14,950	15,564	15,663	14,754	16,902	21,807	13,932 ^a
S9	3,307	3,376	2,673	2,773	2,361	2,204	2,780	2,784	2,691	2,823	3,880	3,640 ^a
C1	1,099	1,161	2,078	1,993	1,298	1,288	1,492	1,480	1,407	1,479	2,091	556 ^a
C2	160	125	314	297	132	115	202	179	174	147	321	158 ^a
A1	9,590	8,673	9,065	8,352	6,511	5,911	8,389	7,646	7,260	8,156	10,788	8076 ^a
SP1	1,310	1,362	1,125	1,220	930	956	1,121	1,179	1,135	1,148	1,836	830 ^b
SP2	8,004	8,487	7,675	7,790	8,409	8,514	8,029	8,264	7,844	8,992	12,226	7,584 ^b
SP3	25,836	24,145	24,848	23,696	25,101	25,087	25,262	24,309	22,865	27,240	36,983	26,362 ^b
SP4	4,179	3,679	4,179	4,422	4,179	3,668	4,179	3,923	3,755	3,872	5,112	2,562 ^b
SP5	13,045	15,052	13,045	14,068	13,045	14,663	13,045	14,594	13,834	16,355	18,112	13,795 ^b
SP6	14,362	15,742	14,362	15,245	14,362	15,602	14,362	15,530	14,708	17,536	19,343	14,741 ^b

^aThe data is cited from Dong and Blunt (2009). ^bThe networks are extracted using the “porennet” (Dong & Blunt, 2009) based on maximal ball algorithm, and the absolute permeability is calculated based on the “poreflow” (Valvatne & Blunt, 2004).

where A_0 and L are the cross-sectional area and the length of porous media, respectively.

The directional permeability along x , y , and z directions is presented in Table 3. The relative errors in the absolute permeability predicted by different types of networks are compared in Figure 6. It is shown that the present method has the highest accuracy in predicting absolute permeability among different segmentation methods. The relative errors in the absolute permeability predicted by WS – HC networks are mostly below 10%, with an average relative error of 5.8%, while those of WS – w networks, WS – α networks, and MB – α networks are 11.4%, 41.4%, and 26.0%, respectively. A slightly lower w in WS – w networks and a slightly higher α in WS – α networks may result in more accurate predictions of the absolute permeability. Although a relative error of 38.5% in absolute permeability predictions has been reported in Youssef’s own work (Youssef et al., 2007), with the tortuosity corrections proposed by this work, the average relative error of WS – Youssef networks for single-phase permeability is reduced down to 6.3% (also see Figure S5 in Supporting Information S1). The good performance of both the present method and the Youssef method results from the idea of the equivalence of flow resistance.

3.3. Two-Phase Flow

3.3.1. Prediction of the Capillary Pressure Curve

The capillary pressure curve is used to verify the accuracy of different segmentation methods. Samples include Bentheimer sandstone and Castlegate sandstone (Shikhov et al., 2017). Information about the two samples is listed in Table 4. The perfect wetting condition, that is, zero contact angle, is adopted in the pore network modeling of drainage. The capillary pressure curves predicted by network types of WS – HC, WS – Youssef, WS – w , and WS – α are compared with the experimental data (mercury intrusion capillary pressure) (Shikhov et al., 2017).

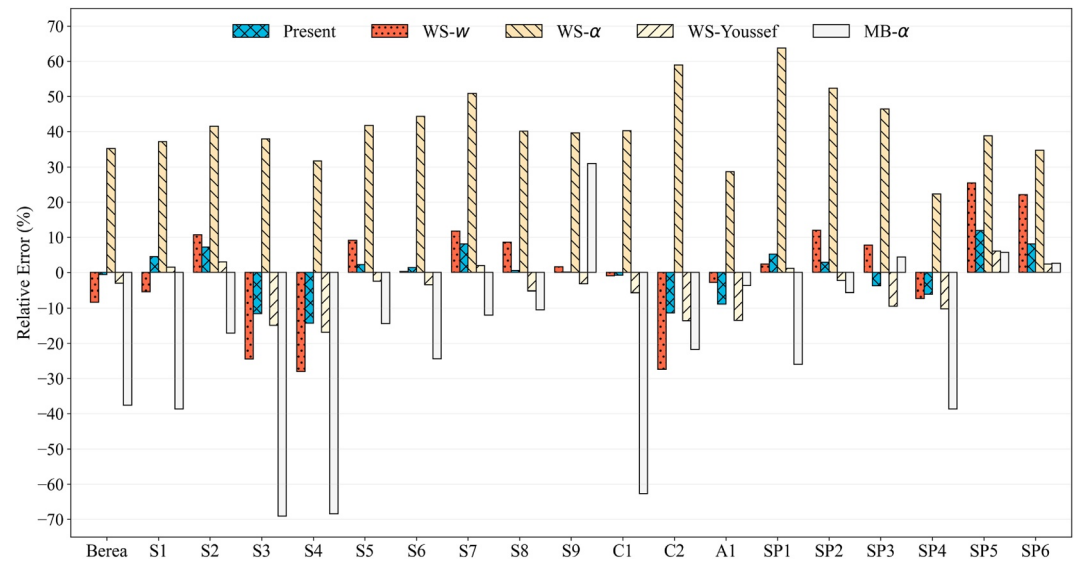


Figure 6. Relative errors in the absolute permeability predicted by different types of pore networks, compared to the direct numerical simulations by LBM. Samples include sandstone (Berea and S1–S9), carbonate (C1–C2), sand pack (A1), and spherical pack (SP1–SP6). The WS – Youssef networks, WS – w networks, and WS – α networks are extracted by the Youssef method, the w method, and the α method coupled with the SNOW algorithm (Gostick, 2017), respectively. The MB – α networks are extracted by the α method coupled with the maximal ball algorithm (Dong & Blunt, 2009).

Both simulated and experimental capillary pressure curves are converted to air-water fluid pairs with the interfacial tension of $72 \text{ mN} \cdot \text{m}^{-1}$. Since the volumes of network elements are identical, the capillary pressure curves predicted by network types of the WS – Youssef, WS – w , and WS – α are exactly the same and collectively referred to as the “other networks,” see Figure S8 in Supporting Information S1.

The predicted capillary pressure curves based on different segmentation methods are almost the same. This is because the mercury intrusion is a bond percolation and the mercury-air interface moves by piston-type displacement. Whenever mercury passes through a throat, it will enter adjacent pores. Therefore, whether the throat volume is zero or not has a negligible effect on the saturation of the wetting phase, and ultimately on the capillary pressure curve. In addition, regardless of the segmentation method, the maximum capillary pressure is underestimated due to the limited resolution of pore structures.

Table 4
Information About the Studied Samples and the Settings in Pore Network Modeling of Imbibition

Samples	Types	Size (voxels)	Resolution (μm)	Wettability condition	Contact angles (degree)	Initial condition	Boundary condition	Porosity (%)
Berea ^a	Sandstone	400 ³	5.345	Water-wet	50 ~ 70	Oil-invaded elements are determined by the primary drainage in pore network modeling.	Water is injected from the left side, and oil has to escape from the right side.	19.6
L1-3 ^b		1,000 × 1,000 × 850	3.92		30 ~ 65			17.2
Bentheimer ^c		800 ³	2.89		55 ~ 65			23.1
Castlegate ^c		800 ³	3.36		50 ~ 65			22.2
Leopard ^c		800 ³	2.15		50 ~ 65			20.3
Gildehause ^d		893 × 897 × 566	4.4		50 ~ 55			20.0
Ketton ^e	Limestone	1,189 × 1,163 × 1,000	3.28	Strongly water-wet	40 ~ 55	Oil-invaded elements are mapped from the CT image of the drainage experiment.	Water is injected from the top and bottom sides simultaneously, and oil can escape from either side.	23.0

^aThe core sample is quoted from Dong and Blunt (2009). ^bA sandstone sample from Daqing oilfield in China. ^cThe core samples are quoted from Shikhov et al. (2017). ^dThe core sample is quoted from Rucker et al. (2015). ^eThe core sample is quoted from Singh et al. (2017).

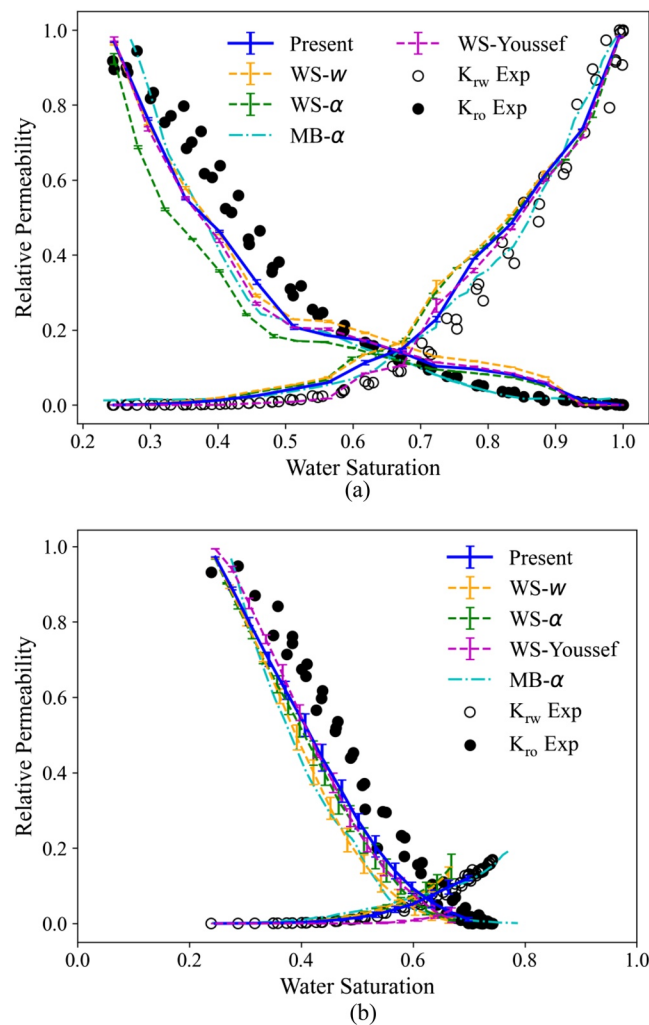


Figure 7. The predicted relative permeability curves during (a) primary drainage and (b) imbibition for Berea sandstone. The results of pore network modeling are compared with the experimental data by Oak (1990). The WS – Youssef networks, WS – w networks, and WS – α networks are extracted by the Youssef method, the w method, and the α method coupled with the SNOW algorithm (Gostick, 2017), respectively. The MB – α data is referenced from Dong and Blunt (2009).

3.3.2. Prediction of Relative Permeability Curves

The accuracy of the present method is further verified by relative permeability curves. The quasi-static pore network modeling is performed on seven core samples, including sandstone and limestone (Dong & Blunt, 2009; Rücker et al., 2015; Shikhov et al., 2017; Singh et al., 2019). The predicted relative permeability curves are compared with the experimental data (Bultreys et al., 2020; Oak, 1990; Shikhov et al., 2017). Information on the core samples and the simulation settings are summarized in Table 4.

For each of the cases, 10 simulations are performed on our household program, a secondary development based on the framework of OpenPNM (Gostick et al., 2016). Network elements are uniform ducts with circular, triangular, or square cross-sectional shapes, which are characterized by the dimensionless shape factor G (Mason & Morrow, 1991). Pore-scale displacement mechanisms include piston-type displacement, snap-off, and cooperative filling (Valvatne & Blunt, 2004). Wettability effects such as fractional wetting, contact angle hysteresis, and wetting layers are considered. The contact angle hysteresis is mimicked by the Class III model proposed by Morrow (1975). The two-phase simulation algorithm will not be described too much here. For details, please refer to Valvatne and Blunt (2004).

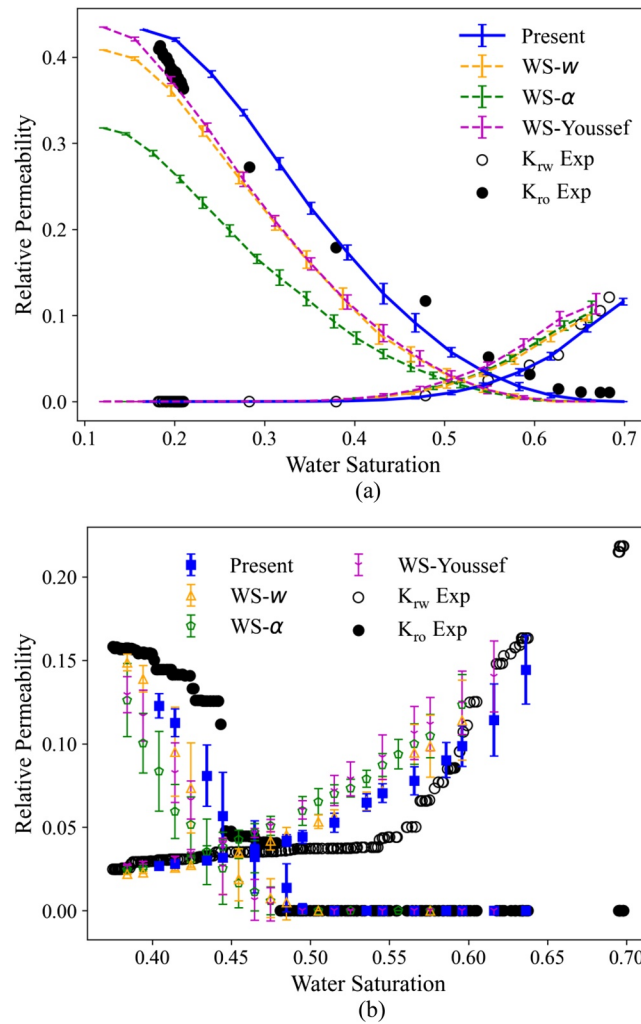


Figure 8. The predicted relative permeability curves during imbibition for (a) Gildehauser sandstone and (b) Ketton limestone. The WS – Youssef networks, WS – w networks, and WS – α networks are extracted by the Youssef method, the w method, and the α method coupled with the SNOW algorithm (Gostick, 2017), respectively. The experimental results are quoted from Bultreys et al. (2020).

The relative permeability curves predicted by different types of networks are compared with the experimental data in Figures 7–9. The relative permeability curves predicted by WS – w networks and WS – α networks are in reasonable agreement with the experimental data but not good. Except for the cases of Gildehauser sandstone and Ketton limestone, WS – Youssef networks significantly underestimate the relative permeability of water during imbibition. Generally, WS – HC networks predict the relative permeability curves in better agreement with the experimental data than the other types of networks. Pore-throat segmentation has a significant impact on the predicted two-phase transport properties, as shown in Text 4 in Supporting Information S1. The same conclusion was also reached in previous studies (Bondino et al., 2013; Idowu et al., 2013). This is the reason why the proper assignment of a boundary between a pore and a throat has been emphasized in numerous studies (Bhattad et al., 2011; Bondino et al., 2013; Gostick, 2017; Idowu et al., 2013; Raeini et al., 2017; Xiong et al., 2016). The better performance of WS – HC networks results from the physics-based pore-throat segmentation which leads to a physical definition of lengths and volumes of network elements. On the one hand, WS – HC networks predict more accurate absolute permeability under the saturated condition and phase permeability under unsaturated conditions than the other types of networks, which has been discussed in Section 3.2. Consequently, WS – HC networks predict more accurate relative permeability which is the phase permeability divided by the absolute permeability. On the other hand, WS – HC networks predict more accurate saturation than the other types of

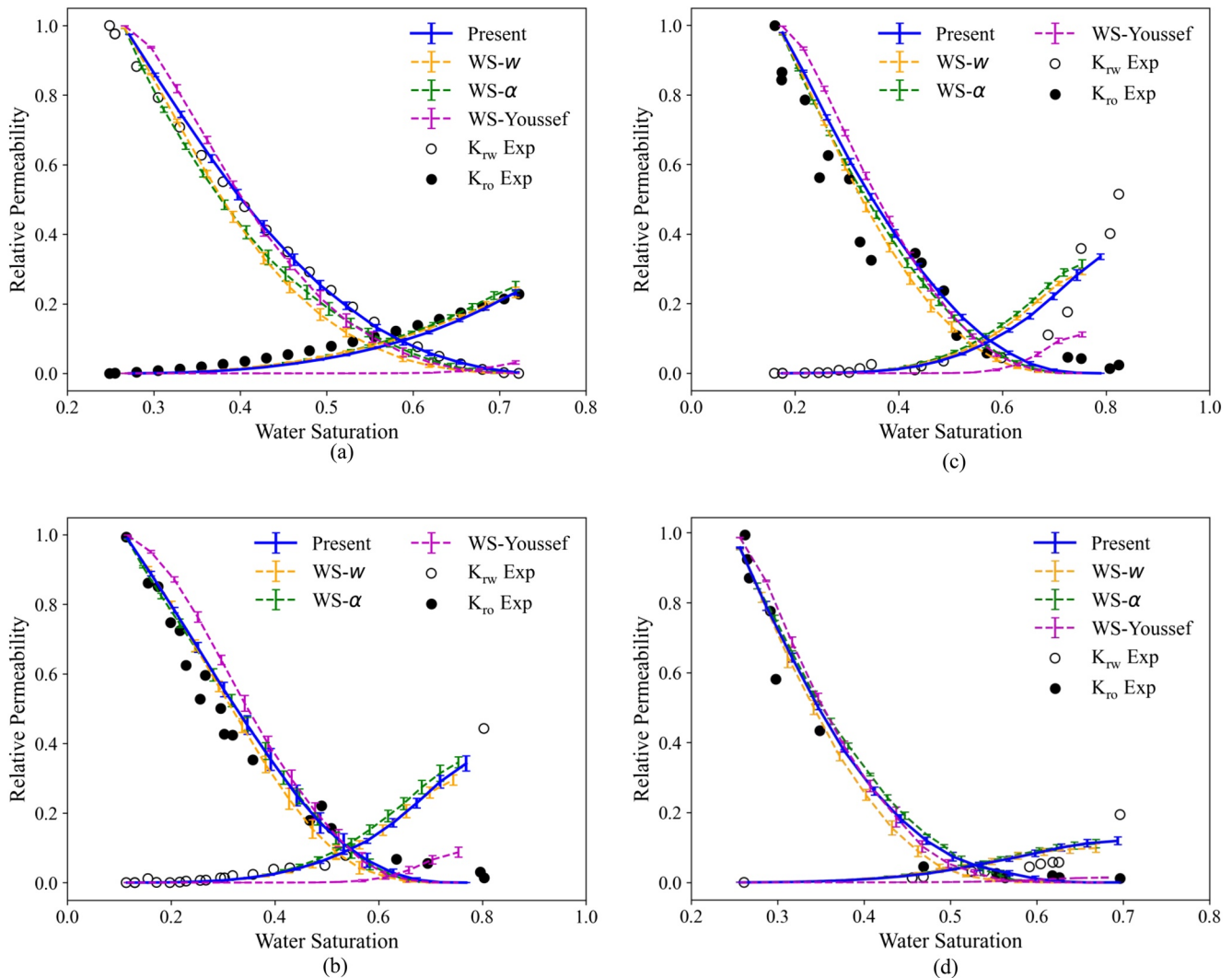


Figure 9. The predicted relative permeability curves during imbibition for (a) L1-3 sandstone from Daqing oilfield in China, (b) Bentheimer sandstone, (c) Castlegate sandstone, and (d) Leopard sandstone. The WS – Youssef networks, WS – w networks, and WS – α networks are extracted by the Youssef method, the w method, and the α method coupled with the SNOW algorithm (Gostick, 2017), respectively. The experimental data of the L1-3 sandstone is obtained by a steady state measurement, while the experimental data of the Bentheimer sandstone, the Castlegate sandstone, and the Leopard sandstone are quoted from Shikhov et al. (2017).

networks due to the physical definition of volumes of network elements. With the more accurate calculation of relative permeability and saturation, WS – HC networks predict the relative permeability curves in better agreement with the experimental data than the other types of networks.

4. Conclusions

This study has proposed a pore-throat segmentation method based on local hydraulic resistance equivalence between the real space and the pore-throat geometry. The method determines the pore-throat boundary at the position where the simplified tubes preserve the local hydraulic resistance of the real space best. This pore-throat segmentation method ensures a better equivalency between extracted pore network and real pore space without any empirical and non-physical parameters. After validations of accuracy and reliability by standard benchmarks, this method is applied to 25 samples of real porous materials, and the prediction results are compared with those by the previous segmentation methods, including the WS – Youssef method, the WS – w method, the WS – α method, and the MB – α method. Significant differences in conduit lengths and volumes of network elements

have been found for the extracted pore networks with different segmentation methods. The single-phase transport property, like absolute permeability, and the two-phase transport properties, such as the relative permeability curves and the capillary pressure curves, have been predicted and compared with the DNS results and the experimental data. The results demonstrate that the proposed method exhibits the best performance in accuracy among different segmentation methods. The increase of computational costs by local hydraulic resistance equivalence calculations is slight, and the overall computational cost of the proposed PNM is negligible compared with any DNS methods. Although the proposed pore-throat segmentation method based on local hydraulic resistance equivalence is still limited to a low Reynolds number, it provides a possibility to enhance the capability of PNM to capture geometry variations of pore space and extend PNM to more complicated applications, such as fluid-solid coupling and reactive transport in porous media.

Data Availability Statement

The data in the study are available at Mendeley Data via <https://data.mendeley.com/datasets/td6w86djr9/1> with open access. The open-source code for pore-throat segmentation is available at Mendeley Data via <https://data.mendeley.com/datasets/mwsxdb2tpm/3>.

Acknowledgments

This work is financially supported by the National Key Research and Development Program of China (No. 2019YFA0708704) and the NSF grant of China (Nos. 12272207, U1837602).

References

- Alizadeh, A., Jin, X., & Wang, M. R. (2019). Pore-scale study of ion transport mechanisms in inhomogeneously charged nanoporous rocks: Impacts of interface properties on macroscopic transport. *Journal of Geophysical Research-Solid Earth*, *124*(6), 5387–5407. <https://doi.org/10.1029/2018jb017200>
- Al-Kharusi, A. S., & Blunt, M. J. (2007). Network extraction from sandstone and carbonate pore space images. *Journal of Petroleum Science and Engineering*, *56*(4), 219–231. <https://doi.org/10.1016/j.petrol.2006.09.003>
- Arand, F., & Hesser, J. (2017). Accurate and efficient maximal ball algorithm for pore network extraction. *Computers & Geosciences*, *101*, 28–37. <https://doi.org/10.1016/j.cageo.2017.01.004>
- Bhattad, P., Willson, C. S., & Thompson, K. E. (2011). Effect of network structure on characterization and flow modeling using X-ray micro-tomography images of granular and fibrous porous media. *Transport in Porous Media*, *90*(2), 363–391. <https://doi.org/10.1007/s11242-011-9789-7>
- Blunt, M. J. (2017). *Multiphase flow in permeable media: A pore-scale perspective*. Cambridge University Press.
- Blunt, M. J., Bijeljic, B., Dong, H., Gharbi, O., Iglauer, S., Mostaghimi, P., et al. (2013). Pore-scale imaging and modelling. *Advances in Water Resources*, *51*, 197–216. <https://doi.org/10.1016/j.advwatres.2012.03.003>
- Bondino, I., Hamon, G., Kallel, W., & Kac, D. (2013). Relative permeabilities from simulation in 3D rock models and equivalent pore networks: Critical review and way forward. *Petrophysics-The SPWLA Journal of Formation Evaluation and Reservoir Description*, *54*(06), 538–546.
- Bultreys, T., Lin, Q., Gao, Y., Raeini, A. Q., AlRatrou, A., Bijeljic, B., & Blunt, M. J. (2018). Validation of model predictions of pore-scale fluid distributions during two-phase flow. *Physical Review*, *97*(5), 053104. <https://doi.org/10.1103/physreve.97.053104>
- Bultreys, T., Singh, K., Raeini, A. Q., Ruspini, L. C., Øren, P. E., Berg, S., et al. (2020). Verifying pore network models of imbibition in rocks using time-resolved synchrotron imaging. *Water Resources Research*, *56*(6), e2019WR026587. <https://doi.org/10.1029/2019wr026587>
- Chatzis, I., & Dullien, F. A. (1977). Modelling pore structure by 2-D and 3-D networks with application to sandstones. *Journal of Canadian Petroleum Technology*, *16*(01). <https://doi.org/10.2118/77-01-09>
- Chen, S., & Doolen, G. D. (1998). Lattice Boltzmann method for fluid flows. *Annual Review of Fluid Mechanics*, *30*(1), 329–364. <https://doi.org/10.1146/annurev.fluid.30.1.329>
- Chen, S., Jiang, J., & Guo, B. (2021). A pore-network-based upscaling framework for the nanoconfined phase behavior in shale rocks. *Chemical Engineering Journal*, *417*, 129210. <https://doi.org/10.1016/j.cej.2021.129210>
- Chen, Y., Valocchi, A. J., Kang, Q., & Viswanathan, H. S. (2019). Inertial effects during the process of supercritical CO₂ displacing brine in a sandstone: Lattice Boltzmann simulations based on the continuum-surface-force and geometrical wetting models. *Water Resources Research*, *55*(12), 11144–11165. <https://doi.org/10.1029/2019wr025746>
- Chiogna, G., & Rolle, M. (2017). Entropy-based critical reaction time for mixing-controlled reactive transport. *Water Resources Research*, *53*(8), 7488–7498. <https://doi.org/10.1002/2017wr020522>
- Dong, H., & Blunt, M. J. (2009). Pore-network extraction from micro-computerized-tomography images. *Physical Review*, *80*(3), 036307. <https://doi.org/10.1103/physreve.80.036307>
- Dzwinel, W., & Yuen, D. A. (2000). Matching macroscopic properties of binary fluids to the interactions of dissipative particle dynamics. *International Journal of Modern Physics C*, *11*(01), 1–25. <https://doi.org/10.1142/s012918310000002x>
- Ferrari, A., & Lunati, I. (2014). Inertial effects during irreversible meniscus reconfiguration in angular pores. *Advances in Water Resources*, *74*, 1–13. <https://doi.org/10.1016/j.advwatres.2014.07.009>
- Gerke, K. M., Sidle, R. C., & Mallants, D. (2015). Preferential flow mechanisms identified from staining experiments in forested hillslopes. *Hydrological Processes*, *29*(21), 4562–4578. <https://doi.org/10.1002/hyp.10468>
- Gerke, K. M., Sizonenko, T. O., Karsanina, M. V., Lavrukhin, E. V., Abashkin, V. V., & Korost, D. V. (2020). Improving watershed-based pore-network extraction method using maximum inscribed ball pore-body positioning. *Advances in Water Resources*, *140*, 103576. <https://doi.org/10.1016/j.advwatres.2020.103576>
- Gholipour, H., Kermani, M. J., & Zamanian, R. (2021). Coupled pore network model for the cathode gas diffusion layer in PEM fuel cells. *Acta Mechanica Sinica*, *37*(2), 331–348. <https://doi.org/10.1007/s10409-020-01005-7>
- Godinho, J. R., Gerke, K. M., Stack, A. G., & Lee, P. D. (2016). The dynamic nature of crystal growth in pores. *Scientific Reports*, *6*(1), 1–7. <https://doi.org/10.1038/srep33086>

- Gostick, J. T. (2017). Versatile and efficient pore network extraction method using marker-based watershed segmentation. *Physical Review*, *96*(2), 023307. <https://doi.org/10.1103/physreve.96.023307>
- Gostick, J. T., Aghighi, M., Hinebaugh, J., Tranter, T., Hoeh, M. A., Day, H., et al. (2016). OpenPNM: A pore network modeling package. *Computing in Science & Engineering*, *18*(4), 60–74. <https://doi.org/10.1109/mcse.2016.49>
- Gostick, J. T., Khan, Z. A., Tranter, T. G., Kok, M. D., Agnaou, M., Sadeghi, M., & Jervis, R. (2019). PoreSpy: A python toolkit for quantitative analysis of porous media images. *Journal of Open Source Software*, *4*(37), 1296. <https://doi.org/10.21105/joss.01296>
- Huppert, H. E., & Neufeld, J. A. (2014). The fluid mechanics of carbon dioxide sequestration. In S. H. Davis & P. Moin (Eds.) *Annual review of fluid mechanics* (Vol. 46, pp. 255–272).
- Idowu, N., Nardi, C., Long, H., Øren, P. E., Bondino, I., & Total, E. (2013). Improving digital rock physics predictive potential for relative permeabilities from equivalent pore networks. *Paper SCA*, *17*, 16–19.
- Jerauld, G., & Salter, S. (1990). The effect of pore-structure on hysteresis in relative permeability and capillary pressure: Pore-level modeling. *Transport in Porous Media*, *5*(2), 103–151. <https://doi.org/10.1007/bf00144600>
- Lindquist, W. B., Lee, S. M., Coker, D. A., Jones, K. W., & Spanne, P. (1996). Medial axis analysis of void structure in three-dimensional tomographic images of porous media. *Journal of Geophysical Research*, *101*(B4), 8297–8310. <https://doi.org/10.1029/95jb03039>
- Liu, F., & Wang, M. (2020). Review of low salinity waterflooding mechanisms: Wettability alteration and its impact on oil recovery. *Fuel*, *267*, 117112. <https://doi.org/10.1016/j.fuel.2020.117112>
- Mason, G., & Morrow, N. R. (1991). Capillary behavior of a perfectly wetting liquid in irregular triangular tubes. *Journal of Colloid and Interface Science*, *141*(1), 262–274. [https://doi.org/10.1016/0021-9797\(91\)90321-x](https://doi.org/10.1016/0021-9797(91)90321-x)
- Meakin, P., & Tartakovsky, A. M. (2009). Modeling and simulation of pore-scale multiphase fluid flow and reactive transport in fractured and porous media. *Reviews of Geophysics*, *47*(3), RG3002. <https://doi.org/10.1029/2008rg000263>
- Mehmani, Y., & Xu, K. (2022). Pore-network modeling of Ostwald ripening in porous media: How do trapped bubbles equilibrate? *Journal of Computational Physics*, *457*, 111041. <https://doi.org/10.1016/j.jcp.2022.111041>
- Morrow, N. R. (1975). The effects of surface roughness on contact: Angle with special reference to petroleum recovery. *Journal of Canadian Petroleum Technology*, *14*(04). <https://doi.org/10.2118/75-04-04>
- Oak, M. (1990). Three-phase relative permeability of water-wet Berea. In *SPE/DOE enhanced oil recovery symposium*. paper presented at.
- Øren, P. E., & Bakke, S. (2003). Reconstruction of Berea sandstone and pore-scale modelling of wettability effects. *Journal of Petroleum Science and Engineering*, *39*(3–4), 177–199. [https://doi.org/10.1016/s0920-4105\(03\)00062-7](https://doi.org/10.1016/s0920-4105(03)00062-7)
- Øren, P. E., Bakke, S., & Arntzen, O. J. (1998). Extending predictive capabilities to network models. *SPE Journal*, *3*(04), 324–336. <https://doi.org/10.2118/52052-pa>
- Patzek, T., & Silin, D. B. (2001). Shape factor and hydraulic conductance in noncircular capillaries: I. One-Phase creeping flow. *Journal of Colloid and Interface Science*, *236*(2), 295–304. <https://doi.org/10.1006/jcis.2000.7413>
- Qin, C. Z., Wang, X., Hefny, M., Zhao, J., Chen, S., & Guo, B. (2022). Wetting dynamics of spontaneous imbibition in porous media: From pore scale to Darcy scale. *Geophysical Research Letters*, *49*(4), e2021GL097269. <https://doi.org/10.1029/2021gl097269>
- Rabbani, A., Jamshidi, S., & Salehi, S. (2014). An automated simple algorithm for realistic pore network extraction from micro-tomography images. *Journal of Petroleum Science and Engineering*, *123*, 164–171. <https://doi.org/10.1016/j.petrol.2014.08.020>
- Raeini, A. Q., Bijeljic, B., & Blunt, M. J. (2017). Generalized network modeling: Network extraction as a coarse-scale discretization of the void space of porous media. *Physical Review*, *96*(1), 013312. <https://doi.org/10.1103/physreve.96.013312>
- Ramstad, T., Øren, P. E., & Bakke, S. (2010). Simulation of two-phase flow in reservoir rocks using a lattice Boltzmann method. *SPE Journal*, *15*(04), 917–927. <https://doi.org/10.2118/124617-pa>
- Rubol, S., Battiato, I., & de Barros, F. P. J. (2016). Vertical dispersion in vegetated shear flows. *Water Resources Research*, *52*(10), 8066–8080. <https://doi.org/10.1002/2016wr018907>
- Rücker, M., Berg, S., Armstrong, R., Georgiadis, A., Ott, H., Schwing, A., et al. (2015). From connected pathway flow to ganglion dynamics. *Geophysical Research Letters*, *42*(10), 3888–3894. <https://doi.org/10.1002/2015gl064007>
- Sheppard, A., Sok, R., & Averdunk, H. (2005). Improved pore network extraction methods. In *International symposium of the society of core analysts*. paper presented at.
- Sheppard, A., Sok, R., Averdunk, H., Robins, V., & Ghous, A. (2006). Analysis of rock microstructure using high-resolution X-ray tomography. In *Proceedings of the international symposium of the society of core analysts*. The Society of Core Analysts Dublin. paper presented at.
- Shikhov, I., d'Eurydice, M. N., Arns, J.-Y., & Arns, C. H. (2017). An experimental and numerical study of relative permeability estimates using spatially resolved T1- ρ NMR. *Transport in Porous Media*, *118*(2), 225–250. <https://doi.org/10.1007/s11242-017-0855-7>
- Sholokhova, Y., Kim, D., & Lindquist, W. B. (2009). Network flow modeling via lattice-Boltzmann based channel conductance. *Advances in Water Resources*, *32*(2), 205–212. <https://doi.org/10.1016/j.advwatres.2008.10.016>
- Silin, D. B., Jin, G., & Patzek, T. W. (2003). Robust determination of the pore space morphology in sedimentary rocks. In *SPE annual technical conference and exhibition*. paper presented at.
- Singh, K., Jung, M., Brinkmann, M., & Seemann, R. (2019). Capillary-dominated fluid displacement in porous media. In S. H. Davis & P. Moin (Eds.), *Annual review of fluid mechanics* (Vol. 51, pp. 429–449).
- Singh, K., Menke, H., Andrew, M., Lin, Q., Rau, C., Blunt, M. J., & Bijeljic, B. (2017). Dynamics of snap-off and pore-filling events during two-phase fluid flow in permeable media. *Scientific Reports*, *7*(1), 1–13. <https://doi.org/10.1038/s41598-017-05204-4>
- Šmilauer, V., Catalano, E., Chareyre, B., Dorofeenko, S., Duriez, J., Dyck, N., et al. (2015). Yade documentation. In *The Yade project* (2nd ed.). Porous Media.
- Sochi, T. (2013). Newtonian flow in converging-diverging capillaries. *International Journal of Modeling, Simulation, and Scientific Computing*, *4*(03), 1350011. <https://doi.org/10.1142/s1793962313500116>
- Tartakovsky, A. M., Meakin, P., Scheibe, T. D., & Wood, B. D. (2007). A smoothed particle hydrodynamics model for reactive transport and mineral precipitation in porous and fractured porous media. *Water Resources Research*, *43*(5), W05437. <https://doi.org/10.1029/2005wr004770>
- Thompson, K. E., Willson, C. S., White, C. D., Nyman, S., Bhattacharya, J. P., & Reed, A. H. (2008). Application of a new grain-based reconstruction algorithm to microtomography images for quantitative characterization and flow modeling. *SPE Journal*, *13*(02), 164–176. <https://doi.org/10.2118/95887-pa>
- Tranter, T. G., Gostick, J. T., Burns, A. D., & Gale, W. F. (2018). Capillary hysteresis in neutrally wettable fibrous media: A pore network study of a fuel cell electrode. *Transport in Porous Media*, *121*(3), 597–620. <https://doi.org/10.1007/s11242-017-0973-2>
- Valvatne, P. H., & Blunt, M. J. (2004). Predictive pore-scale modeling of two-phase flow in mixed wet media. *Water Resources Research*, *40*(7), W07406. <https://doi.org/10.1029/2003wr002627>
- Wang, C., Wu, K., Scott, G. G., Akisanya, A. R., Gan, Q., & Zhou, Y. (2020). A new method for pore structure quantification and pore network extraction from SEM images. *Energy & Fuels*, *34*(1), 82–94. <https://doi.org/10.1021/acs.energyfuels.9b02522>

- Wang, Z., & Battiato, I. (2020). Patch-based multiscale algorithm for flow and reactive transport in fracture-microcrack systems in shales. *Water Resources Research*, *56*(2), e2019WR025960. <https://doi.org/10.1029/2019wr025960>
- Xie, C., Lei, W., Balhoff, M. T., Wang, M., & Chen, S. (2021). Self-adaptive preferential flow control using displacing fluid with dispersed polymers in heterogeneous porous media. *Journal of Fluid Mechanics*, *906*, A10. <https://doi.org/10.1017/jfm.2020.763>
- Xie, C., Raeini, A. Q., Wang, Y., Blunt, M. J., & Wang, M. (2017). An improved pore-network model including viscous coupling effects using direct simulation by the lattice Boltzmann method. *Advances in Water Resources*, *100*, 26–34. <https://doi.org/10.1016/j.advwatres.2016.11.017>
- Xiong, Q., Baychev, T. G., & Jivkov, A. P. (2016). Review of pore network modelling of porous media: Experimental characterisations, network constructions and applications to reactive transport. *Journal of Contaminant Hydrology*, *192*, 101–117. <https://doi.org/10.1016/j.jconhyd.2016.07.002>
- Yang, Y., Zhang, X., Tian, Z., Deissmann, G., Bosbach, D., Liang, P., & Wang, M. (2022). Thermodiffusion of ions in nanoconfined aqueous electrolytes. *Journal of Colloid and Interface Science*, *619*, 331–338. <https://doi.org/10.1016/j.jcis.2022.03.077>
- Yi, Z., Lin, M., Jiang, W., Zhang, Z., Li, H., & Gao, J. (2017). Pore network extraction from pore space images of various porous media systems. *Water Resources Research*, *53*(4), 3424–3445. <https://doi.org/10.1002/2016wr019272>
- Youssef, S., Rosenberg, E., Gland, N., Bekri, S., & Vizika, O. (2007). Quantitative 3D characterisation of the pore space of real rocks: Improved μ -CT resolution and pore extraction methodology. *International Sympo of the Society of Core Analysts*, 17.
- Zhao, H. Q., Macdonald, I. F., & Kwiecien, M. J. (1994). Multi-orientation scanning: A necessity in the identification of pore necks in porous media by 3-D computer reconstruction from serial section data. *Journal of Colloid and Interface Science*, *162*(2), 390–401. <https://doi.org/10.1006/jcis.1994.1053>
- Zheng, D., Wang, W., & Reza, Z. (2019). Pore-network extraction algorithm for shale accounting for geometry-effect. *Journal of Petroleum Science and Engineering*, *176*, 74–84. <https://doi.org/10.1016/j.petrol.2019.01.046>
- Zheng, J., Ju, Y., & Wang, M. (2018). Pore-scale modeling of spontaneous imbibition behavior in a complex shale porous structure by pseudopotential lattice Boltzmann method. *Journal of Geophysical Research-Solid Earth*, *123*(11), 9586–9600. <https://doi.org/10.1029/2018jb016430>